Corresponding author:

Dr. Jenny Q. Du

Department of Electrical and Computer Engineering

Mississippi State University

Mississippi State, MS 39762

phone: 662-325-2035

fax: 662-325-2298

e-mail: du@ece.msstate.edu

Dependent Component Analysis for Blind Restoration of Images Degraded by Turbulent Atmosphere

Qian Du [1], Ivica Kopriva [2]

[1] Department of Electrical and Computer Engineering

Mississippi State University, MS 39762, USA

[2] Division of Laser and Atomic Research and Development, Rudjer Bošković Institute

Bijenička cesta 54, P.O. Box 180, 10002 Zagreb, Croatia

Abstract

In our previous research, we applied independent component analysis (ICA) for the restoration of image sequences degraded by atmospheric turbulence. The original high-resolution image and turbulent sources were considered independent sources from which the degraded image is composed of. Although the result was promising, the assumption of source independence may not be true in practice. In this paper, we propose to apply the concept of dependent component analysis (DCA), which can relax the independence assumption, to image restoration. In addition, the restored image can be further enhanced by employing a recently developed Gabor-filter-bank-based single channel blind image deconvolution algorithm. Both simulated and real data experiments demonstrate that DCA outperforms ICA, resulting in the flexibility in the use of adjacent image frames. The contribution of this research is to convert the original multi-frame blind deconvolution problem into blind source separation problem without

the assumption on source independence; as a result, there is no *a priori* information, such as sensor bandwidth, point-spread-function, or statistics of source images, that is required.

1. Introduction

Atmospheric turbulence is an inevitable problem in long-distance ground-based and space-based imaging. The optical effects of atmospheric turbulence arise from random inhomogeneities in the temperature distribution of the atmosphere. A consequence of these temperature inhomogeneities is non-stationary random distribution of the refraction index of the atmosphere [1]. Atmospheric turbulence can make distant objects being viewed through a sensor (e.g., a digital camera or video recorder) to appear blurred. Also, the time-varying nature of the turbulence can make the appearance of objects to wave in a slow quasi-periodic fashion. When a target is small and moving, its actual location becomes very difficult to estimate. This phenomenon greatly hinders accurate target detection, tracking, classification, and identification.

Numerous methods have been developed to mitigate the atmospheric turbulence effects. Three broad classes of techniques used to correct turbulence effects are: 1) pure post-processing techniques, which use specialized image processing algorithms; 2) adaptive optics techniques, which afford a mechanical means of sensing and correcting for turbulence effects; and 3) hybrid methods, which combine the elements of post-processing techniques and adaptive optics techniques. Each of these techniques has performance limitation as well as hardware and software requirements. In our research, due to its low cost, we focus on the development of pure

post-processing techniques to correct atmospheric turbulence. Quite a few algorithms in this aspect have been developed in the past twenty years. These algorithms fall into two major categories: those adopting explicit or implicit ways to measure the perturbations induced on the wavefront by the atmosphere, and those using no wavefront information to construct the underlying image formation characteristics of the atmosphere. Wavefront reference algorithms include the guides (natural or artificial) and deconvolution from optical measurements of the wavefront entering the telescope, while reference-less algorithms do not need such guides. In our research, we are interested in the no-reference techniques because no optical measurements are required. This also makes real time or near-real time implementation possible and simple for many national defense related applications.

Current image restoration techniques for atmospheric turbulence correction employ the well-known linear image formation model $g(x,y) = h(x,y) * s(x,y)$, where the degraded image $g(x,y)$ is obtained by convolving the original high-resolution image $s(x,y)$ with the point-spread-function (PSF) $h(x,y)$ (i.e., PSF models the degradation caused by atmospheric turbulence) [2]. Due to the space- and time-varying nature of atmospheric turbulence, the PSF should be changed with pixel location (x,y) and time t. However, for the purpose of simplicity and mathematical tractability, most techniques assume that PSF is unchanged with space and time. In other words, they are space- and time-invariant restoration approaches.

To relax the unrealistic assumption of a space- and time-invariant PSF, we introduced the Blind Source Separation (BSS) technique to achieve the restoration of image sequences [3]. Instead of using the linear convolutive degradation model and estimating the PSF, we considered each spatial turbulence pattern as one physical source, the original high-resolution image of the

4

object as another source, and then the degraded low-resolution image was the result from the linear combination of these sources. This leads to the model at the component level written as

$$g(x,y,t_n) = \sum_{m=1}^{M} a_{nm}(\Delta t_n) s_m(x,y,t_0) \tag{1}$$

where contributions from the high-resolution object image and individual turbulence patterns $\{s_m\}_{m=1}^{M}$ between time t_n and the reference time t_0, i.e. $\Delta t_n = t_n - t_0$, are contained in the unknown mixing matrix coefficients a_{nm}, which depend on some physical constants [3]. The component level model (1) can be generalized to a multi-frame model in a matrix form as

$$\mathbf{G} = \mathbf{AS} \tag{2}$$

where $\mathbf{G} \in R^{N \times T}$ is a matrix of the blurred image frames with each row representing a blurred image frame, $\mathbf{A} \in R^{N \times M}$ is an unknown basis or mixing matrix, and $\mathbf{S} \in R^{M \times T}$ is a matrix of the source images. Here, N represents the number of frames whereas each frame is treated as one measurement, M denotes the number of source images, and $T = P \times Q$ stands for the number of pixels in each image (P and Q are image spatial dimensions). It is assumed that each image frame has been transformed into a vector by a row or column stacking procedure. It is also assumed that motion effects, if present, are compensated in advance.

BSS can be applied on (2) to extract the high-resolution object image without the prior knowledge or estimation of PSF. The most successful solution of the BSS problem is achieved through independent component analysis (ICA). It solves the BSS problem by imposing a constraint on extracted sources to be non-Gaussian (at most one source is allowed to be Gaussian) and statistically independent from each other [4]. One of popular ICA algorithms, referred to as Joint Approximate Dia-gonalization of Eigenmatrices (JADE), was adopted due to

its robustness, wherein the statistical dependence among data samples was measured by the fourth-order cross-cumulants [5].

However, it has been argued that the assumption of source independence may not be true in many situations. For instance, the atmospheric turbulence components may be correlated spatially and temporally. Sources may be at least partially statistically dependent due to the fact that multi-frame image model adopted in [3] and used herein assumes all the sources are emitted from the same space-time location (x, y, t_0). Thus, in this paper, we will propose the use of dependent component analysis (DCA) for image restoration, which does not require sources to be independent. Both simulated and real data experiments demonstrate that DCA outperforms ICA under this circumstance. In addition, DCA can be employed to further sharpen the restored image to achieve super-resolution.

In summary, the contribution of this research is to convert the original multi-frame blind deconvolution problem into BSS problem without the assumption on source independence; as a result, no *a priori* information or assumption on sensor bandwidth, PSF, or statistics of source images is required.

2. Derivation of DCA algorithms

Few papers in the literature discuss the problem of DCA [6]. Here we adopt some previous studies conducted in [7][8]. The basic idea behind DCA is to find a transform T that can improve the statistical independence between the sources but leave the basis matrix unchanged, i.e.,

$$T(\mathbf{G}) = T(\mathbf{AS}) \cong \mathbf{A}T(\mathbf{S}). \tag{3}$$

Because the sources after this transformation will be less statistically dependent, any standard ICA algorithm, such as JADE, derived for the original BSS problem can be used to learn the

basis matrix **A**. Once the basis matrix **A** is estimated, the sources **S** can be recovered by applying the pseudo-inverse of **A** on the multi-frame image **G** in (2).

Examples of linear transforms that possess such a required invariance property and generate less dependent sources include: 1) highpass filtering, 2) innovation, and 3) wavelet transforms.

Highpass filtering (HP)

A highpass filter, such as the Butterworth highpass filter, is applied to preprocess the observed signals **G**, followed by a standard ICA algorithm, such as JADE, on the filtered data in order to learn the mixing matrix **A**. This is motivated by the fact that highpass filtered signals are usually more independent than original signals that include low frequency components. Meanwhile, this approach is computationally very efficient, making it attractive for DCA problems with statistically dependent sources. In this case the transform T in Eq. (3) is the highpass filtering operator that can be seen as a special case of the filter bank approach [9][10].

Innovation (IN)

Another computationally efficient approach is based on the use of innovation. The arguments for using innovation are that they are usually more independent from each other and more non-Gaussian than original processes [11]. The innovation process is referred to as prediction error [12], which is defined as:

$$e_m(r) = s_m(r) - \sum_{i=1}^{l} b_i s_m(r-i), \quad m = 1, \cdots, M \tag{4}$$

where $s_m(r-i)$ is the i-th sample of a source process $s_m(r)$ at location $(r-i)$ and b's are prediction coefficients. $e_m(r)$ represents the new information that $s_m(r)$ has but is not contained in the past l

samples. It is proved in [11] that if **G** and **S** follow the linear mixture model (2) their innovation processes $\mathbf{E_G}$ and $\mathbf{E_S}$ (in matrix form) follow the same model as well, i.e.,

$$\mathbf{E_G} = \mathbf{AE_S}. \tag{5}$$

In this case the transform T in Eq. (3) is the linear prediction operator. Temporal decorrelation based preprocessing algorithm [23] can be seen as an extension of the presented innovation based DCA algorithm. It is the same as the presented method when the model is linear but the algorithm in [23] works in the case of post-nonlinear mixture as well.

Subband decomposition independent component analysis (SDICA)

The SDICA approach assumes that wideband source signals can be dependent but some of their narrowband sub-components are less dependent [9][10]. Thus, SDICA extends applicability of standard ICA through the relaxation of the independence assumption. In this case, the transform T in Eq. (3) is any kind of filter-bank-like transform used to implement the sub-band decomposition scheme.

A wavelet transform-based approach to SDICA was developed in [8][13] to obtain adaptive subband decomposition of wideband signals through a computationally efficient implementation in a form of iterative filter bank. Computationally efficient small cumulant-based approximation of mutual information is used for automated selection of the subband with the least dependent components, to which an ICA algorithm is applied. The potential disadvantage of this approach is high computational complexity if 2D wavelet transform is used for image decomposition. Hence, a reformulation can be accomplished based on dual tree complex wavelets [14]. Dual tree complex wavelets are approximately computationally as efficient as decimated wavelet packets but as accurate as the shift-invariant wavelet packet approach [15][16].

3. Algorithms for comparison

Other BSS approaches that can deal with statistically dependent sources include: independent subspace analysis (ISA) [24][25], nonnegative matrix and tensor factorization (NMF/NTF) [27-30], and the blind Richardson-Lucy (BRL) algorithm [33-36], which are used for comparison purpose in this paper. They are briefly described as follows.

Independent Subspace Analysis

ISA assumes that the source signal space is composed of a number of subspaces. Signals contained in the same subspace are mutually dependent while signals contained in different subspaces are independent. When each subspace contains one component only, the ISA becomes ICA. The practical difficulty with the ISA approach is in choosing a scheme necessary to partition the source signal space into the subspaces with the required property. For instance, it is not obvious how to choose the number of subspaces as well as the number of signals contained in each subspace.

In the multi-frame blind deconvolution problem treated in this paper we decompose the signal space into two subspaces: one that contains one image representing an approximation of the object and the other that contains images related to the turbulence patterns. Here, we present in the sequel brief derivation of the ISA algorithm [25], which is based on the concept of multi-dimensional ICA [24] that follows the same model in (2). It is assumed that components $\{\mathbf{s}_m\}_{m=1}^{M}$ are divided into K tuples where components contained in the same tuple are dependent and components contained in different tuples are independent (in other words, tuples correspond to subspaces). It is also assumed in [25] that the joint probability density function (pdf) of a particular subspace is spherically symmetric; hence, it can be expressed as the sum of squares of

$\left\{\mathbf{s}_i^k\right\}_{i=1}^{d_k}$, where k denotes the subspace index and d_k denotes the dimension of the kth subspace such that $\sum_{k=1}^{K} d_k = M$. It is further assumed sparse representation, which may be in agreement with data representation adopted in our approach due to the fact that turbulence patterns are expected to be sparse. Under these assumptions the following gradient update for de-mixing matrix $\mathbf{W}$ is obtained (i.e., $\mathbf{WG} \approx \mathbf{S}$)

$$\Delta \mathbf{w}_m(t) \propto -\mathbf{z}(t) s_m(t) \left(\sum_{i \in S_{k(m)}} \left(s_i(t) \right)^2 \right)^{-\frac{1}{2}} \quad m = 1,...,M \tag{6}$$

where $k(m)$ denotes the index of the subspace to which $\mathbf{w}_m$ belongs and $\mathbf{z}$ denotes the whitened data (whitening is applied to data matrix in ISA in the same way as in standard ICA) [26].

Nonnegative Matrix and Tensor Factorization

Unlike ICA, NMF/NTF algorithms do not impose statistical independence or non-Gaussianity requirements on the sources. NMF/NTF algorithms may yield physically useful solutions by imposing the nonnegativity, sparseness or smoothness constraints on the sources [27-30]. In [27], the NMF algorithm was first derived to minimize two cost functions: the squared Euclidean distance and the Kullback-Leibler divergence. Using a gradient descent approach the resulting multiplicative algorithms converged very slowly. In addition, the lack of additional constraints prevents NMF algorithms [27] from yielding a unique decomposition. Generalization of the NMF algorithms [27] has been done in [28-30]. The gradient-based NMF algorithm with a sparseness constraint being incorporated into the cost function leads to the regularized alternating least square (RALS) algorithm [28]:

$$D\left(\mathbf{G} \| \mathbf{AS}\right) = \frac{1}{2} \|\mathbf{G} - \mathbf{AS}\|^2 + \alpha_{\mathbf{S}} \Phi_{\mathbf{S}}(\mathbf{S}) + \alpha_{\mathbf{A}} \Phi_{\mathbf{A}}(\mathbf{A}) \tag{7}$$

where the regularization terms α_S and α_A enforce sparse solutions for **A** and **S**, respectively. If constraints are chosen as $\left[\Phi_S(S)\right]_{ij} = 1/2\,s_{ij}^2$ and $\left[\Phi_A(A)\right]_{ij} = 1/2\,a_{ij}^2$, the regularization terms help regularize the pseudo-inverse when the normal matrices $\mathbf{A}^T\mathbf{A}$ and $\mathbf{SS}^T$ are ill-conditioned. Assume $\nabla_S D(\mathbf{G}\|\mathbf{AS}) = \mathbf{0}$ and $\nabla_A D(\mathbf{G}\|\mathbf{AS}) = \mathbf{0}$ for positive entries in **A** and **S,** which occurs at stationary points. Then

$$\mathbf{S}^{(k+1)} = \max\left\{\varepsilon, \left(\mathbf{A}^T\mathbf{A} + \alpha_S^{(k)}\right)^+ \mathbf{A}^T\mathbf{G}\right\}\bigg|_{\mathbf{A}=\mathbf{A}^{(k)}}$$

$$\mathbf{A}^{(k+1)} = \max\left\{\varepsilon, \mathbf{GS}^T\left(\mathbf{SS}^T + \alpha_A^{(k)}\right)^+\right\}\bigg|_{\mathbf{S}=\mathbf{S}^{(k+1)}} \tag{8}$$

where k denotes iteration index, $(\ )^+$ is Moore-Penrose inverse, and ε is a small constant (10^{-9}) to enforce positive entries. Regularization terms help avoid local minima and are implemented as $\alpha_A^{(k)} = \alpha_S^{(k)} = \alpha_0 \exp(-k/\tau)$ (in the experiments α_0=20 and τ=10). We employ constraints if there is *a priori* information about the sparseness of either **A** or **S**; otherwise, we set both regularization terms to zero. This algorithm is referred to as the NMF algorithm in this paper.

Extension of this approach, known as local ALS, to 3D tensor factorization is given in [29], which is referred to as the NTF algorithm in this paper. In this case **G** and **S** in model (2) become 3D tensors: $\mathbf{G} \in R_{0+}^{N \times P \times Q}$ and $\mathbf{S} \in R_{0+}^{M \times P \times Q}$. Unlike a majority of NTF/NMF algorithms that estimate the source matrix/tensor globally, the local ALS algorithm [29] performs it at the source level:

$$\left\{\mathbf{s}_m = \left[\mathbf{a}_m^T\mathbf{G}^{(m)} - \alpha_s^{(m)}\right]_+\right\}_{m=1}^M$$

$$\mathbf{A} = \left[\mathbf{A} - (\mathbf{AS} - \mathbf{G})\mathbf{S}^T\left(\mathbf{SS}^T + \lambda\mathbf{I}_M\right)^{-1}\right]_+ \tag{9}$$

where $\mathbf{I}_M$ is an $M \times M$ identity matrix, $\alpha_s^{(m)}$ is a sparseness constraint that regulates sparseness of the mth source, $\mathbf{a}_m$ represents the mth column of **A** , $\mathbf{G}^{(m)} = \mathbf{G} - \sum_{j \neq m} \mathbf{a}_j\mathbf{s}_j$, and $[\xi]_+ = \max\{\varepsilon, \xi\}$

(e.g., $\xi=10^{-16}$). Regularization constant λ changes as a function of the iteration index as $\lambda_k = \lambda_0 \exp(-k/\tau)$ (with $\lambda_0 = 100$ and $\tau = 0.02$ in the experiments). Note that sparseness constraint $\alpha_s^{(m)}$ imposed on source tensors affects the final result ($\alpha_s^{(m)} = 0.05$ in the experiment).

Blind Richardson-Lucy (BRL) algorithm

BRL algorithm [33][34] was originally derived for non-blind single frame deconvolution of astronomical images. It has been later formulated in [35] for blind deconvolution, and then modified by an iterative restoration algorithm in [36]. To briefly introduce BRL algorithm we need to write a single frame image $\mathbf{g}_n$, $n \in \{1,...,N\}$, in the lexicographical notation:

$$\mathbf{g}_n = \mathbf{H}\mathbf{s} \tag{10}$$

where $\mathbf{g}_n$, $\mathbf{s} \in R_{0+}^{PQ}$, $\mathbf{H} \in R_{0+}^{PQ\times PQ}$ (BRL needs to employ a PSF function whose matrix version is $\mathbf{H}$). The observed image vector $\mathbf{g}_n$ and the original image vector $\mathbf{s}$ are obtained by a stacking procedure. The matrix $\mathbf{H}$ is a block-Toeplitz matrix [31]. It absorbs itself into the blurring kernel $h(x,y)$ by assuming that at least its size is known. The block-Toeplitz structure of $\mathbf{H}$ can be further approximated by a block-circular structure. This approximation introduces small degradations at image boundaries, but enables the expression of Eq. (10) with the circular convolution. The algorithm can be implemented in the block adaptive fashion:

$$\hat{\mathbf{H}}_{i+1}^{(k)} = \left[\left(\hat{\mathbf{s}}^{(k-1)} \right)^T \left(\mathbf{g} \oslash \left(\hat{\mathbf{H}}_i^k \hat{\mathbf{s}}^{(k-1)} \right) \right) \right] \hat{\mathbf{H}}_i^{(k)}$$

$$\hat{\mathbf{s}}_{i+1}^{(k)} = \left[\hat{\mathbf{s}}_i^{(k)} \otimes \left(\mathbf{H}^{(k)\mathrm{T}} \left(\mathbf{g} \oslash \left(\mathbf{H}^{(k)} \hat{\mathbf{s}}_i^{(k)} \right) \right) \right) \right] \tag{11}$$

where $\otimes$ denotes component-wise multiplication, $\oslash$ denotes component-wise division, i and k are internal and main iteration indices, respectively. Note that although $\mathbf{H}$ is blindly estimated from the observed image, its size must be either known or estimated *a priori*.

4. DCA for single image enhancement

After a high-resolution frame is reconstructed, its quality can be further improved using a sharpening approach in a post-processing step. In general, it is difficult to conduct image sharpening based on a single-frame image only, due to the lack of additional information. It is easier if more observations are available about the scene, and image details can be extracted from these observations. Here, we investigate a single-frame multi-channel image enhancement approach [13]. A 2D Gabor filter bank can be employed to realize multi-channel filtering, considered as multiple observations for ICA or DCA [13]. After the multi-channel version of the original image is generated, an ICA or DCA algorithm can be applied to extract an enhanced image. The multi-channel linear mixture model of an observed image, in the form of (2), has in [13] been obtained under a special assumption that source signals are the original high-resolution source image and its higher order spatial derivatives. Note that this special class of sources is mutually statistically dependent, [17], and a DCA algorithm is a better choice than an ICA algorithm to fulfill image enhancement.

5. No-reference image quality assessment

In order to objectively evaluate image quality after restoration, automatic assessment is needed. When desired high-resolution image is available, quality assessment can simply be achieved by comparing the restored image with desired image using a certain criterion, such as signal-to-noise ratio (SNR). However, in many practical situations the desired image is not available. Thus, quality assessment becomes "no-reference". Here we introduce two "no-reference" metrics: the area under the magnitude of the 1D the Fourier transform along a chosen line in the image and the Laplacian operator.

The power spectrum-based image quality metric has been proposed in [21][22] due to the invariance of power spectra of arbitrary scenes. It has been proposed as a substitute for subjective image assessment in situations when naturally occurring targets are not available and when re-imaging of the same scene for comparison purpose (via mean square error) is not possible. Most importantly the power spectrum metric can be easily incorporated into a human visual system model [21][22]. In this paper, instead of calculating power spectrum-based image quality metric in an absolute sense, we compare one-dimensional power spectrums of images restored by various algorithms. When the power spectrum is normalized to unit gain at the DC component, the area under it corresponds to the level of details contained in the image:

$$PSA = \sum_{\omega=0}^{\Omega} \frac{|F(\omega)|}{|F(0)|} \tag{12}$$

where Ω corresponds with half of the sampling frequency and $|F(\omega)|$ represents magnitude of the discrete Fourier transform (DFT) of a chosen line in the image. An image with better quality of restored details should have a larger *PSA*.

The Laplacian operator is an approximation to the second derivative of brightness *I(x,y)* in direction *x* and *y*, can be applied:

$$\nabla^2 I(x, y) = \frac{\partial I^2(x, y)}{\partial x^2} + \frac{\partial I^2(x, y)}{\partial y^2}. \tag{13}$$

It is actually a spatial highpass filter. It yields a larger response to a point than to a line. An image with turbulence is typically comprised of points varying in brightness, and the Laplacian operator will emphasize these points. A metric based on Laplacian operator is [18]

$$I_4 = \text{mean}\left(\left|\nabla^2 I(x, y)\right|\right) \tag{14}$$

14

which takes the average of second-order derivatives of pixels in the entire image. An image with better quality should have a smaller I_4.

6. Experiments

6.1 Computer simulation

In order to perform comparative performance analysis and demonstrate performance consistency of the DCA algorithms in solving blind deconvolution problem, we created four degraded frames. They were obtained by convolving the original image shown in Fig. 1(a) (with 128×128 pixels) using a Gaussian kernel-based PSFs, i.e.

$$g_n(x,y) = h_n(x,y,\sigma_n) * s(x,y) \quad n = 1,...,4$$

$$h_n(x,y,\sigma_n) = C_n \exp\left(-\frac{x^2 + y^2}{2\sigma_n^2}\right) \tag{15}$$

where C_n and σ_n represent a normalization constant and standard deviation associated with the nth frame, respectively.

We point out that Gaussian kernel-based PSFs are commonly used to simulate the long-term exposure to atmospheric turbulence [31][32]. Standard deviations used to generate four PSFs in this experiment were randomly chosen as [1.8535 2.1909 2.2892 1.9624]. Fig. 1(b) shows one of the four blurred frames. Fig. 2 shows the result obtained by DCA (IN-JADE) algorithm. Based on the adopted data representation one image (i.e., Fig. 2(b)) corresponds with the object, while the rest of images correspond with turbulence patterns. Fig. 3 shows the restored images using various algorithms. In terms of visual perception, the best performance is achieved by innovation and HPF based DCA algorithms. Note that performance of the BRL algorithm is modest despite the fact that radius of the degradation kernel had to be estimated. To quantify the performance,

Table 1 lists the values using the two no-reference image quality metrics: *PSA* metric given by Eq. (12) and I_4 metric given by Eq. (14). Note that better performance corresponds to a larger *PSA* value and a smaller I_4 value. In this regard it appears that DCA algorithms based on innovation, HP filtering, and wavelet transform performed the best. This is in agreement with the visual impression discussed previously.

6.2 Real data experiment 1

An image sequence of the Washington Monument is used in the experiment, which is the same as in [3]. Note that the frames with 10-frame spacing were used in [3]. In Figs. 4-12, we compared the performance of the ICA (i.e., JADE) algorithm and the three DCA algorithms in nine cases with different fashions in frame selection. The number of Givens rotations was used to evaluate the computational complexity, and the Laplacian metric I_4 was adopted to evaluate the image quality.

Case 1: using 5 consecutive frames (Fig. 4)

In this case, the observations were obviously dependent. So the JADE algorithm yielded a poor result. The three DCA algorithms provided better performance, but the result could be further improved. This may be because the number of frames (i.e., observations) was not large enough to accommodate all the sources existing (the number of components that can be extracted is up-bounded by the number of frames).

Case 2: using 10 consecutive frames (Fig. 5)

In this case, the observations were strongly dependent. So the JADE algorithm yielded an even poorer result. Compared to Case 1, the three DCA algorithms provided better performance with the number of frames (i.e., observations) being increased.

16

Case 3: using 20 consecutive frames (Fig. 6)

The phenomenon was similar to that in Case 2. The performance of the JADE algorithm became worse, and the performance of the three DCA algorithms became better.

Case 4: using 50 consecutive frames (Fig. 7)

The phenomenon was similar to that in Case 2. The performance of the JADE algorithm became even worse, and the performance of the three DCA algorithms became even better.

Case 5: using 25 frames with 2-frames spacing (Fig. 8)

In this case, the observations became less dependent. But the performance of the three DCA algorithms was still better than that of the JADE algorithm.

Case 6: using 10 frames with 5-frames spacing (Fig. 9)

In this case, the observations became more independent. The performance of the JADE algorithm became much better, and the performance of the three DCA algorithms remained unchanged.

Case 7: using 20 frames with 5-frames spacing (Fig. 10)

It is similar to Case 6 but more frames were used. The performance of the JADE algorithm became worse again due to the increase of the number of frames; the performance of the three DCA algorithms was slightly improved.

Case 8: using 10 frames with 10-frames spacing (Fig. 11)

In this case, the observations became quite independent. The performance of the JADE algorithm became much better; the performance of the three DCA algorithms remained unchanged.

Case 9: using 5 frames with 20-frames spacing (Fig. 12)

In this case, the observations became very independent. So the performance of the JADE algorithm was improved; the performance of the three DCA algorithms remained unchanged.

The observations in Cases 1-9 can be summarized as follows.

1) When the original JADE is applied, use of consecutive frames causes the difficulty in source separation; it has to use the frames with spacing; increasing the number of frames even worsens the situation.

2) The proposed DCA algorithms can relax the constraints on frame selection, greatly simplifying future hardware implementation.

3) Among the three DCA algorithms, the one using innovation provides the best reconstruction result (due to the smallest I_4 values in most cases).

4) Among the three DCA algorithms, the SDICA requires the least computation time (due to the smallest number of Givens rotations in most cases).

5) The three DCA algorithms may yield better results than the original ICA even when the ICA performs well.

Note that increasing the frame spacing results in more independent observations. Consequently, the mixing matrix **A** is better conditioned. This certainly improves the performance of the ICA algorithm. However, the performance of the DCA algorithms is not influenced much by this strategy due to its capability of handling source dependence. However, if spacing is increased too much, then the slow quasi-periodic variation of turbulence can make the measurements more linearly dependent, which will degrade the ICA performance again. Hence, DCA algorithms can significantly relax the constraints on the selection of frames and the number of frames to be used in the restoration process.

The data in Case 1, which includes five consecutive frames, were used for comparative performance analysis with other methods capable to separate dependent sources. The PSA and I_4 were calculated for the restored images obtained from these methods. As shown in Table 2, it is confirmed that ISA, NMF, NTF, and BRL could not compete with the three DCA methods. Within the three DCA methods, those using innovation and HP filtering provided the best results.

Fig. 13 shows an original image obtained after restoration with the previously described DCA approach. Fig. 14 shows the 16 versions (real and imaginary) obtained after 2D Gabor filtering where two spatial frequencies and four orientations were used [13]. Then there were 17 channels available for the further processing.

The 17 channels ought to be processed by DCA, because the high-resolution image and its spatial derivatives are statistically dependent [13][17]. One extracted source will be the final sharpened image. In order to automatically extract the finally enhanced image, predictability metric is adopted as the selection criteria. Predictability metric of an extracted image $s(n)$ is defined as:

$$F\left(\{s(n)\}\right) = \log \frac{V\left(\{s(n)\}\right)}{U\left(\{s(n)\}\right)} = \log \frac{\sum_{n}^{n_{\max}} \left(\overline{s}(n) - s(n)\right)^2}{\sum_{n}^{n_{\max}} \left(\tilde{s}(n) - s(n)\right)^2} \qquad (16)$$

where V reflects the extent to which $s(n)$ is predicted by a long term moving average $\overline{s}(n)$ and U reflects the extent to which $s(n)$ is predicted by a short term moving average $\tilde{s}(n)$ [19][20]. Because the deconvolution method [13] extracts source image and its spatial derivatives, the true source image should be the most predictable and its derivatives should be less predictable. In other words, the algorithm automatically chooses the source with the lowest F value as the final sharpened image.

Fig. 15(a) shows the result when the wavelet transform was applied for DCA (i.e., SDICA). Obviously, the final result was s_1. Fig. 16(b) shows the result when the innovation was applied for DCA. Obviously, the final result was still s_1. Comparing the s_1 in Fig. 15(b) with the s_1 in Fig. 15(a), it implies that the result obtained by innovation was better because it looked more natural, and the enhancement around the window area was obvious. Results shown on Fig. 15(a) and Fig. 15(b) were obtained when four sources were extracted using JADE, i.e., it had been assumed that in addition to the high-resolution image its three spatial derivatives existed in the linear mixture model of the multi-channel single frame image. If only one source was assumed, the result looked even better as shown in Fig. 15(c). By comparing Fig. 15(b) and Fig. 15(c) with Fig. 13, we can see that the image is significantly enhanced with sharpened edges and enhanced details such as the area around the window.

6.3 Real data experiment 2

To further investigate the performance of the DCA algorithms, 10 consecutive frames with 108×108 pixels were used in the second experiment. One of degraded frames was shown in Fig. 16(a). The restored images using JADE, IN-JADE, and HP-JADE were shown in Fig. 16(b)-(d), where the improvement is evident around road lamps. Fig. 16(e) is the enhancement result for the image in Fig. 16(d) using the multi-channel filtering approach in Section 4, where the details in tree profile and road lamp were highlighted.

Table 3 lists the image quality assessment results for all the methods. We can see that ICA (JADE) performed well in this case, and SDICA did not perform as well as ICA. However, IN-JADE and HP-JADE still outperformed the ICA. All these methods provided better results than ISA, NMF, NTF, and BRL.

20

7. Conclusion

In our previous research, we applied ICA for the restoration of image sequences degraded by atmospheric turbulence. The degraded image was assumed to be composed of the original high-resolution image and turbulent sources that exist at the same space-time location (x,y,t_0). The assumption made on the high-resolution image and turbulent sources is that they are mutually statistically independent despite the fact that they are emitted from the same space-time location (x,y,t_0). Although the result was promising, the assumption of source independence may not be true in practice. To make the ICA result acceptable, we need to select frames with certain spacing. This leads to problems in real-time or near real-time implementation. In this paper, we propose to apply DCA, which can relax this requirement. The experimental results using simulated and real data demonstrate that DCA can significantly improve the restoration performance, without imposing any requirement on the selection of frames to be used in the restoration process. They outperform other algorithms that can be applied to dependent sources. Among the three DCA algorithms we discuss here, the ones based on innovation and highpass filtering yield the better results and the SDICA based on wavelet packet requires the smallest computational times. In addition to that, the restored image can be further sharpened through a post-processing step with a single-frame multi-channel blind deconvolution method based on 2D Gabor-filter bank and DCA. It is noteworthy that DCA performs similarly to ICA when the assumption of source independence is satisfied.

References

[1] M. C. Roggemann, B. Welsh, Turbulence Effects on Imaging Systems, CRC Press, Boca Raton, 1996.

[2] S. C. Park, M. K. Park, M. G. Kang, Super-resolution image reconstruction: A technical overview, Signal Processing Magazine 20 (2003) 21-36.

[3] I. Kopriva, Q. Du, H. Szu, W. Wasylkiwskyj, Independent component analysis approach to image sharpening in the presence of atmospheric turbulence, Optics Communications 233 (2004) 7-14.

[4] A. Hyvarinen, J. Karhunen, E. Oja, Independent Component Analysis, John Wiley & Sons, 2001.

[5] J. F. Cardoso, A. Souloumiac, Blind beamforming for non-Gaussian signals, IEE-Proc. F 140 (1993) 362-370.

[6] A. K. Barros, The independence assumption: dependent component analysis, in: Advances in Independent Component Analysis, Springer, London, 2000.

[7] I. Kopriva. Blind Signal Deconvolution as an Instantaneous Blind Separation of Statistically Dependent Sources, Lecture Notes in Computer Science 4666, pp. 504-511, Springer-Verlag, Proceedings of the Seventh International Conference on Independent Component Analysis and Blind Source Separation, eds. M.E. Davies et al., London, UK, September 9-12, 2007.

[8] I. Kopriva, D. Seršić, Wavelet packets approach to blind separation of statistically dependent sources, Neurocomputing 71(2008) 1642-1655.

[9] A. Cichocki, P. Georgiev, Blind source separation algorithms with matrix constraints, IEICE Transactions on Fundamentals of Electronics, Communications and Computer Sciences E86-A (2003) 522-531.

[10] T. Tanaka, A. Cichocki, Subband decomposition independent component analysis and new performance criteria, in: Proc. IEEE Int. Conf. on Acoustics, Speech and Signal Processing (ICASSP 2004), Montreal, Canada, 2004, pp. 541-544.

[11] A. Hyvärinen, Independent component analysis for time-dependent stochastic processes, in: Proceedings of the International Conference on Artificial Neural Networks (ICANN'98), pp. 541-546, Skovde, Sweden, 1998.

[12] S. J. Orfanidis, Optimum Signal Processing – An Introduction, 2nd ed. MacMillan Publishing Comp., New York, 1988.

[13] I. Kopriva, Approach to blind image deconvolution by multiscale subband decomposition and independent component analysis, Journal of Optical Society of America A 24 (2007) 973-983.

[14] I. Kopriva, D. Seršić, Robust Blind Separation of Statistically Dependent Sources Using Dual Tree Wavelets, in: Proceedings of the 2007 IEEE International Image Processing Conference, Vol. I, pp. 433-436, San Antonio, TX, USA, September 16-19, 2007.

[15] N. G. Kingsbury, Complex wavelets for shift invariant analysis and filtering of signals, Appl. Comput. Harmon. Anal. 10 (2001) 234-253.

[16] W. Selesnick, R. G. Baraniuk, N.G. Kingsbury, The dual-tree complex wavelet transform, Signal Processing Magazine 22 (2005) 123-151.

[17] M. B. Priestley, Stochastic Differentiability, in: Spectral Analysis and Time Series, London: Academic Press, 1981, pp.153-154.

[18] J. C. Russ, The Image Processing Handbook, CRC Press, Boca Raton, 1992.

[19] J. V. Stone, Blind source separation using temporal predictability, Neural Computation 13 (2001) 1559-1574.

[20] J. V. Stone, Blind deconvolution using temporal predictability, Neurocomputing 49 (2002) 79-86.

[21] N. B. Hill, B. H. Bouzas, Objective Image Quality Measure Derived from Digital Image Power Spectra, Opt. Eng. **31** (1992) 813-825.

[22] J. A. Saghri, P. S. Cheatham, A. Habibi, Image quality measure based on human visual system model, Opt. Eng. **28** (1989) 813-818.

[23] J. Karvanen, T. Tanaka, Temporal Decorrelation as Preprocessing for Linear and Post-nonlinear ICA, in C.G. Puntonet and A. Prieto (Eds.): ICA 2004, LNCS 3195, pp. 774-781, 2004.

[24] J.-F. Cardoso, Multidimensional independent component analysis, in Proceedings of the 1998 IEEE International Conference on Acoustics, Speech and Signal Processing, Seattle, WA, USA.

[25] A. Hyvärinen, P. Hoyer, Emergence of Phase- and Shift-Invariant Features by Decomposition of Natural Images into Independent Feature Subspaces, Neural Computation **12** (2000) 1705-1720.

[26] http://www.cs.helsinki.fi/u/phoyer/software.html.

[27] D. D. Lee, H. S. Seung, Learning the parts of objects by non-negative matrix factorization," Nature **401** - 6755 (1999) 788-791.

[28] A. Cichocki, R. Zdunek, S. Amari, Csiszár's Divergences for Non-negative Matrix Factorization: Family of New Algorithms, LNCS **3889** (2006) 32-39

[29] A. Cichocki, R. Zdunek, S.I. Amari, Hierarchical ALS Algorithms for Nonnegative Matrix Factorization and 3D Tensor Factorization, LNCS **4666** (2007) 169-176.

[30] A. Cichocki, R. Zdunek, S. Amari, Nonnegative Matrix and Tensor Factorization, IEEE Sig. Proc. Mag. **25** (2008) 142-145.

[31] R. L. Lagendijk, J. Biemond, Iterative Identification and Restoration of Images, KAP, 1991.

[32] P. Campisi, K. Egiazarian, editors, Blind Image Deconvolution p. 8-9, CRC Press, Boca Raton, 2007.

[33] W.H. Richardson, Bayesian-based iterative method of image restoration, J.Opt.Soc. Am. **62** (1972) 55-59.

[34] L. B. Lucy, An iterative technique for rectification of observed distribution, Astron. J. **79** (1974) 745-754.

[35] D. A. Fish, A. M. Brinicombe, E. R. Pike, J. G. Walker, Blind deconvolution by means of the Richardson-Lucy algorithm, J. Opt. Soc. Am. A **12** (1995) 58-65.

[36] D. S. C. Biggs, M. Andrews, Acceleration of iterative image restoration algorithms, Applied Optics **36** (1997) 1766-1775.

List of table captions

Table 1.   No-reference quality assessment for the restored images in the computer simulation.

Table 2.   No-reference quality assessment for the restored images in real data experiment 1.

Table 3.   No-reference quality assessment for the restored images in real data experiment 2.

List of figure captions

Fig. 1.   (a) original image and (b) a degraded image used in computer simulation.

Fig. 2.   Four source images obtained from DCA (IN-JADE) algorithm: (a), (c), and (d) correspond to turbulence patterns, (b) corresponds to the restored image.

Fig. 3.   Images restored from four simulated blurred frames using (a) ICA (JADE), (b) DCA (IN-JADE), (c) DCA (HP-JADE), (d) DCA (SDICA), (e) ISA, (f) NMF, (g) NTF, and (h) BRL algorithms.

Fig. 4.   Restored images from ICA and three DCA algorithms when using 5 consecutive frames.

Fig. 5.   Restored images from ICA and three DCA algorithms when using 10 consecutive frames.

Fig. 6.   Restored images from ICA and three DCA algorithms when using 20 consecutive frames.

Fig. 7.   Restored images from ICA and three DCA algorithms when using 50 consecutive frames.

Fig. 8.   Restored images from ICA and three DCA algorithms when using 25 frames with 2-frames spacing.

Fig. 9.   Restored images from ICA and three DCA algorithms when using 10 frames with 5-frames spacing.

Fig. 10. Restored images from ICA and three DCA algorithms when using 20 frames with 5-frames spacing.

Fig. 11. Restored images from ICA and three DCA algorithms when using 10 frames with 10-frames spacing.

Fig. 12. Restored images from ICA and three DCA algorithms when using 5 frames with 20-frames spacing.

Fig. 13. A reconstructed frame for further enhancement.

Fig. 14. Multi-channel version of the original image in Fig. 13 produced by the 2D Gabor filter bank with two spatial frequencies and four orientations.

Fig. 15. Image enhancement for Fig. 13 using single-frame multi-channel filtering.

Fig. 16. Results for real data experiment 2.

Table 1. No-reference quality assessment for the restored images in computer simulation.

	ICA (JADE)	DCA (IN-JADE)	DCA (HP-JADE)	DCA (SDICA)	ISA	NMF	NTF	BRL
PSA	3.53	3.90	4.44	3.18	2.87	3.44	2.45	2.66
I_4	6.18	2.56	3.66	2.79	4.08	5.21	2.54	3.60

Table 2. No-reference quality assessment for the restored images in real data experiment 1.

	ICA (JADE)	DCA (IN-JADE)	DCA (HP-JADE)	DCA (SDICA)	ISA	NMF	NTF	BRL
PSA	2.74	2.74	2.76	2.73	1.61	2.69	2.73	2.23
I_4	2.06	1.63	1.63	1.82	3.53	2.10	9.10	7.29

Table 3. No-reference quality assessment for the restored images in real data experiment 2.

	ICA (JADE)	DCA (IN-JADE)	DCA (HP-JADE)	DCA (SDICA)	ISA	NMF	NTF	BRL
PSA	6.71	6.99	7.11	5.27	3.94	5.20	3.69	2.63
I_4	2.56	2.52	2.56	3.57	5.26	5.19	4.38	5.19

(a)   (b)

Fig. 1. (a) original image and (b) a degraded image used in computer simulation.

(a)
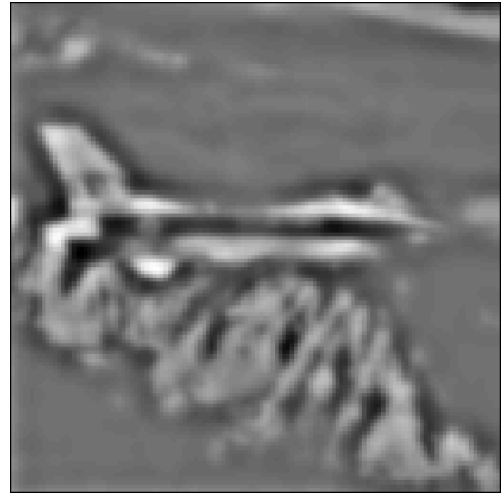
(b)

(c)
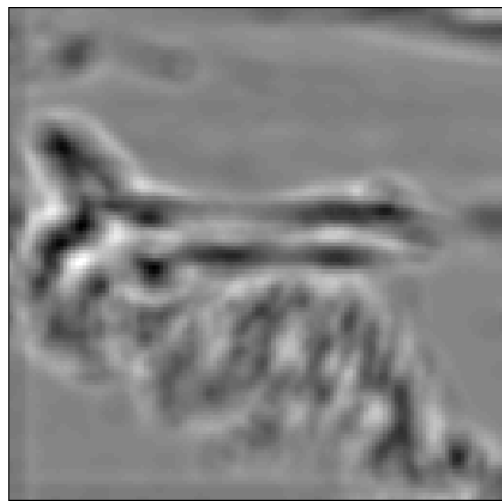
(d)

Fig. 2. Four source images obtained from DCA (IN-JADE) algorithm: (a), (c), and (d) correspond to turbulence patterns, (b) corresponds to the restored image.
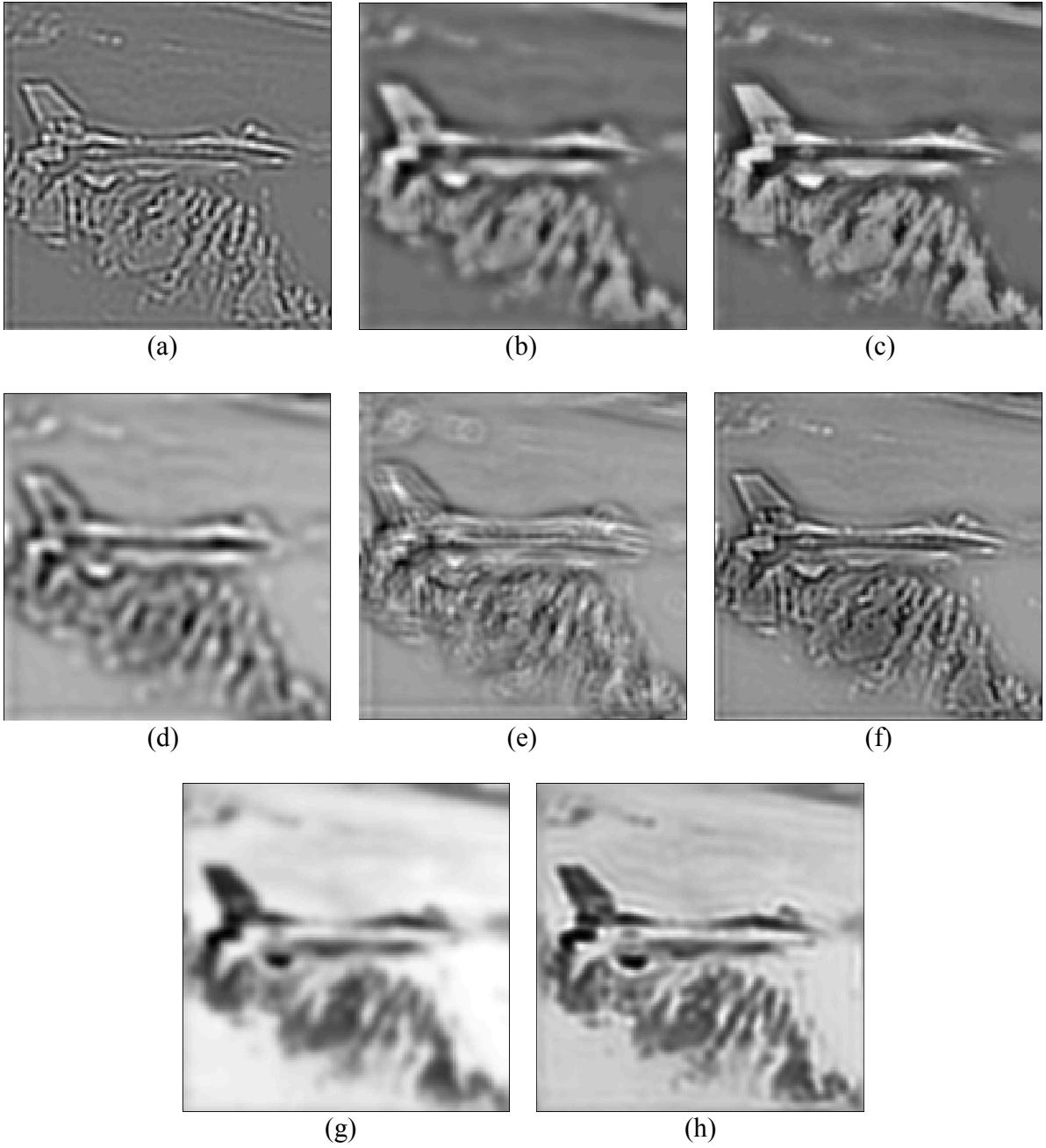
Fig. 3. Images restored from four simulated blurred frames using (a) ICA (JADE), (b) DCA (IN-JADE), (c) DCA (HP-JADE), (d) DCA (SDICA), (e) ISA, (f) NMF, (g) NTF, and (h) BRL algorithms.
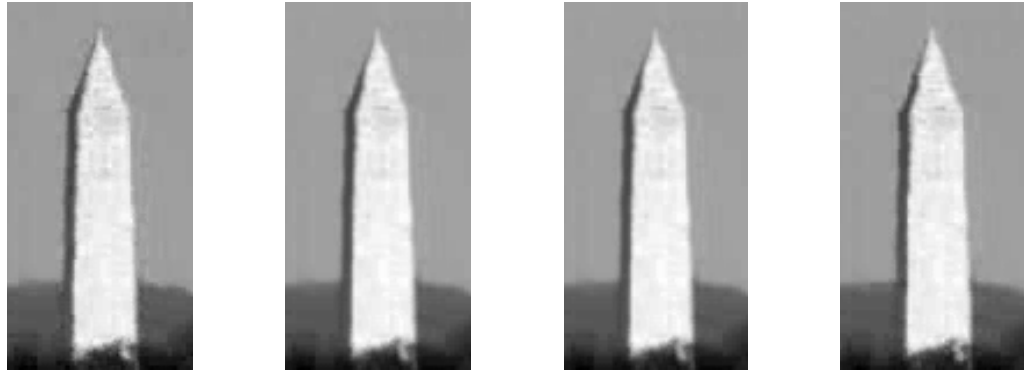
	JADE	HP-JADE	IN-JADE	SDICA
Givens Rotation:	(44)	(30)	(32)	(59)
Laplacian Metric:	(2.0580)	(1.6284)	(1.6260)	(1.8220)

Fig. 4. Restored images from ICA and three DCA algorithms when using 5 consecutive frames.
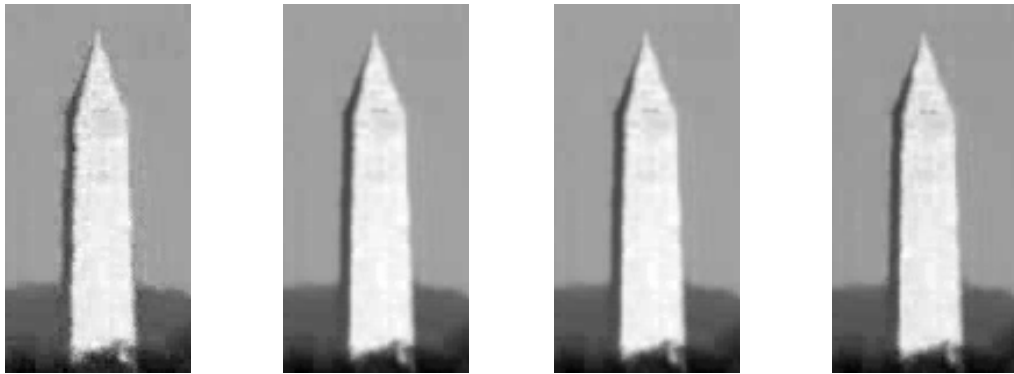
	JADE	HP-JADE	IN-JADE	SDICA
Givens Rotation:	(398)	(265)	(441)	(39)
Laplacian Metric:	(2.3736)	(1.5320)	(1.5236)	(1.6416)

Fig. 5. Restored images from ICA and three DCA algorithms when using 10 consecutive frames.
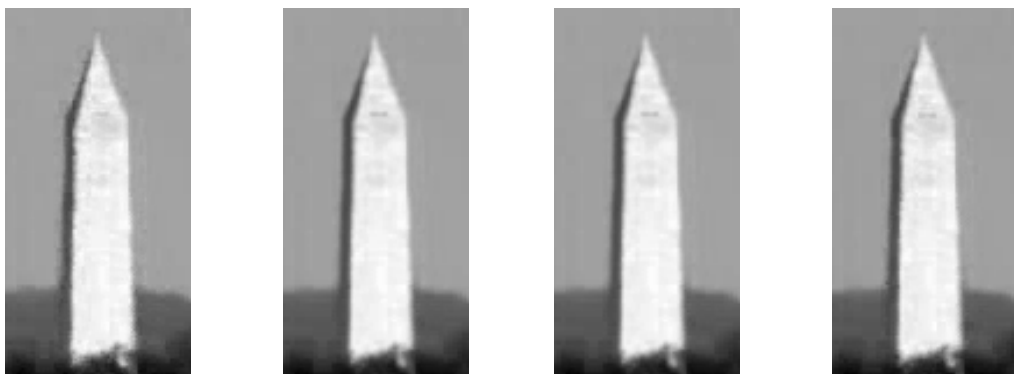
	JADE	HP-JADE	IN-JADE	SDICA
Givens Rotation:	(9341)	(4931)	(3912)	(123)
Laplacian Metric:	(1.9220)	(1.4408)	(1.4328)	(1.6084)

Fig. 6. Restored images from ICA and three DCA algorithms when using 20 consecutive frames.
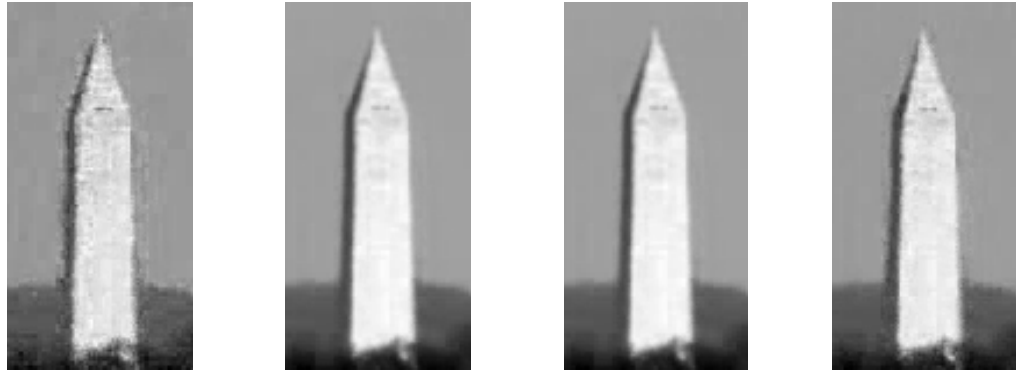
	JADE	HP-JADE	IN-JADE	SDICA
Givens Rotation:	(51746)	(33355)	(36922)	(46)
Laplacian Metric:	(3.4932)	(1.3928)	(1.3756)	(1.5200)

Fig. 7. Restored images from ICA and three DCA algorithms when using 50 consecutive frames.
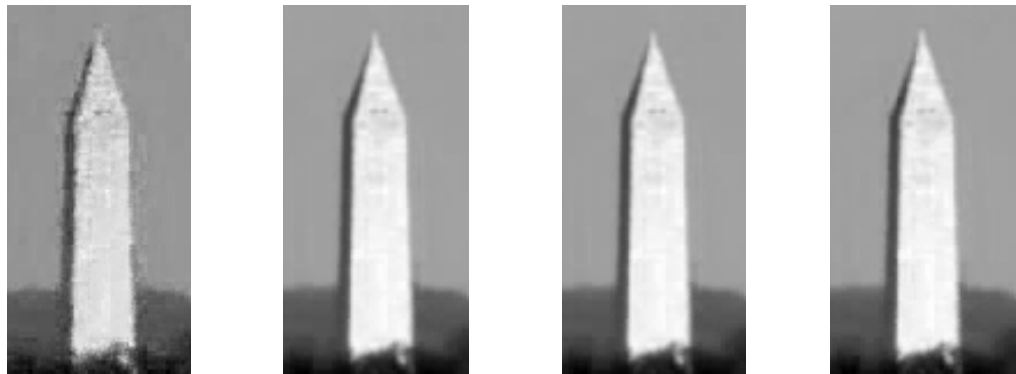
	JADE	HP-JADE	IN-JADE	SDICA
Givens Rotation:	(5364)	(9492)	(8368)	(44)
Laplacian Metric:	(2.8660)	(1.3664)	(1.3600)	(1.4560)

Fig. 8. Restored images from ICA and three DCA algorithms when using 25 frames with 2-frames spacing.
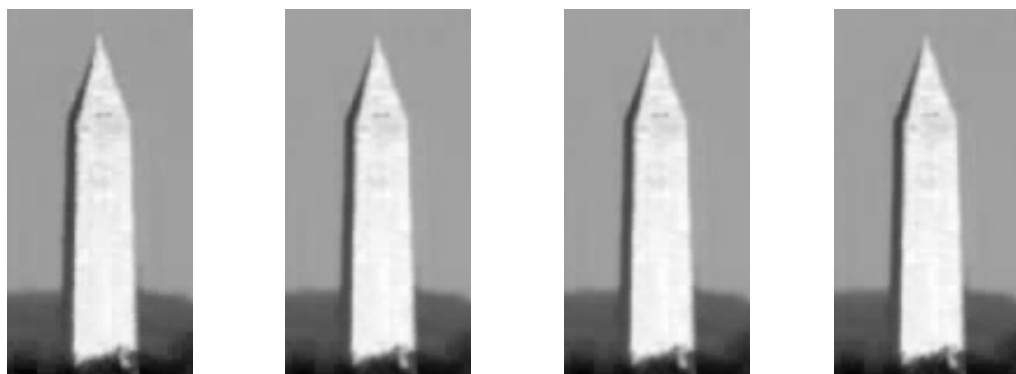
|	JADE	HP-JADE	IN-JADE	SDICA
Givens Rotation:	(715)	(1197)	(460)	(49)
Laplacian Metric:	(1.5192)	(1.3920)	(1.3880)	(1.5448)

Fig. 9. Restored images from ICA and three DCA algorithms when using 10 frames with 5-frames spacing.
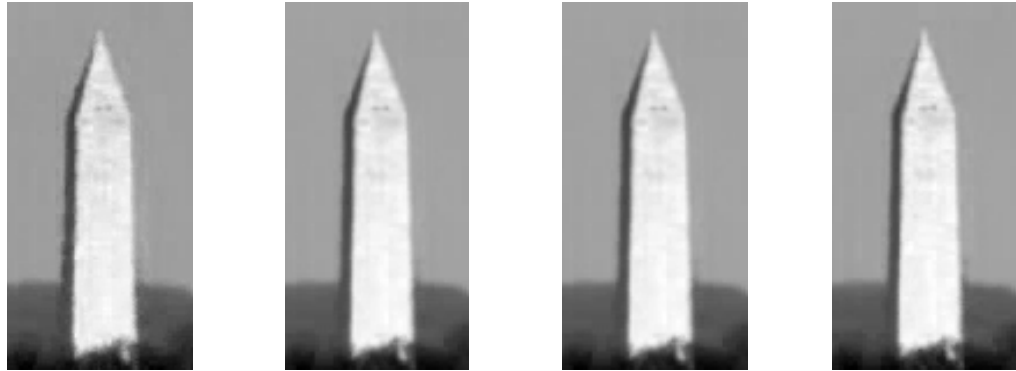
	JADE	HP-JADE	IN-JADE	SDICA
Givens Rotation:	(2224)	(3859)	(4617)	(54)
Laplacian Metric:	(1.8032)	(1.3576)	(1.3456)	(1.4796)

Fig. 10. Restored images from ICA and three DCA algorithms when using 20 frames with 5-frames spacing.
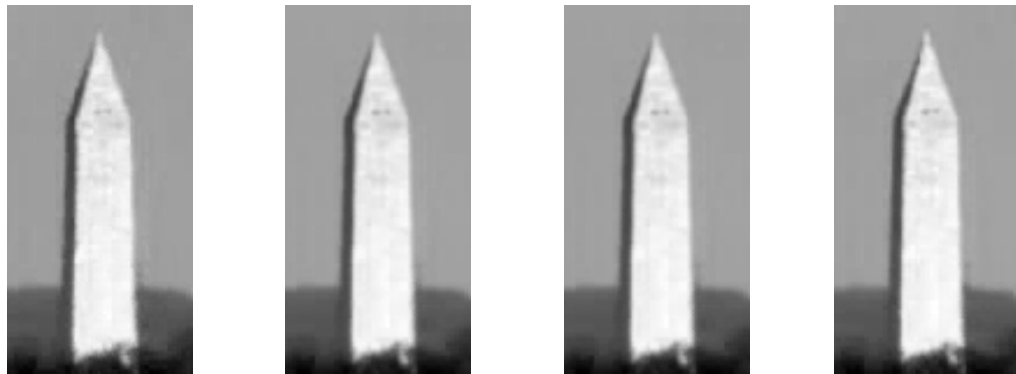
	JADE	HP-JADE	IN-JADE	SDICA
Givens Rotation:	(369)	(254)	(216)	(49)
Laplacian Metric:	(1.6712)	(1.3836)	(1.3828)	(1.3896)

Fig. 11. Restored images from ICA and three DCA algorithms when using 10 frames with 10-frames spacing.
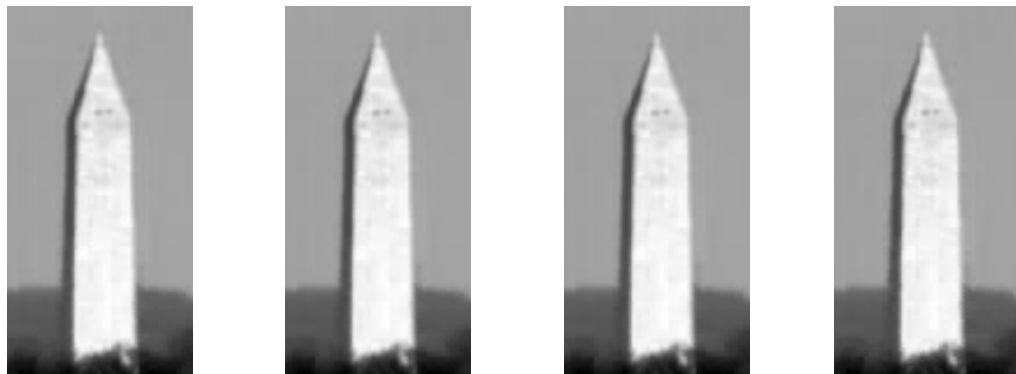
	JADE	HP-JADE	IN-JADE	SDICA
Givens Rotation:	(46)	(40)	(44)	(99)
Laplacian Metric:	(1.4856)	(1.4236)	(1.4248)	(1.5424)

Fig. 12. Restored images from ICA and three DCA algorithms with 20-frames spacing.
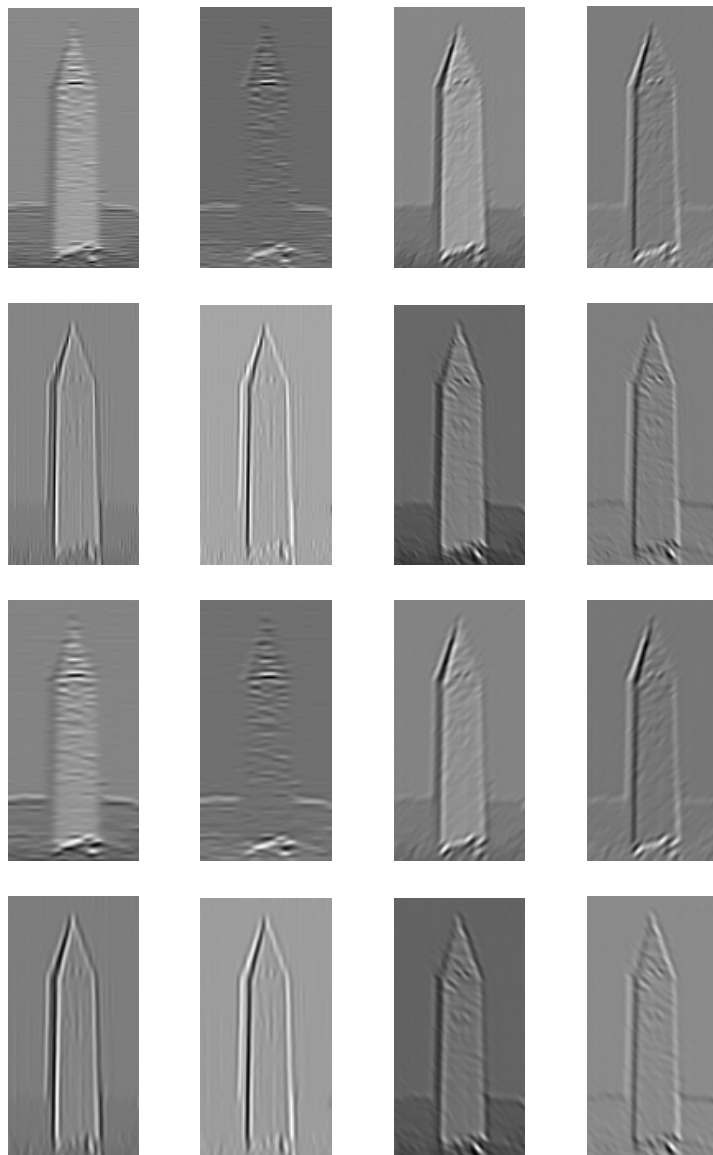
Fig. 13. A reconstructed frame for further enhancement.

Fig. 14. Multi-channel version of the original image in Fig. 13 produced by the 2D Gabor filter bank with two spatial frequencies and four orientations.
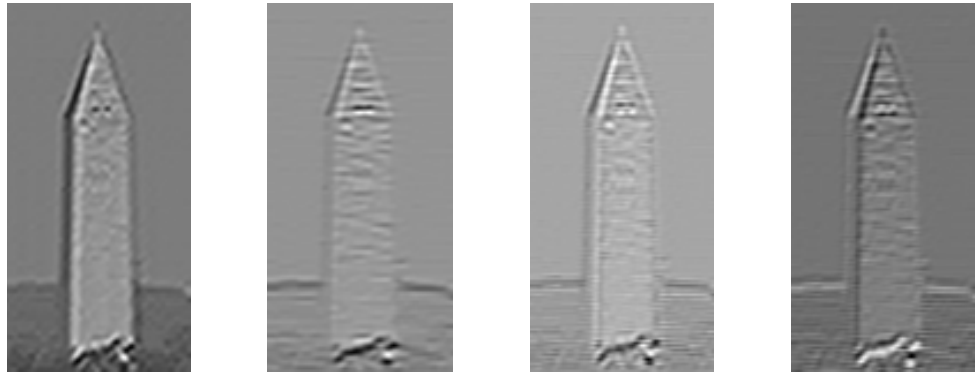
	s_1	s_2	s_3	s_4
Predictability Metric:	(2.4874)	(2.8756)	(2.7367)	(2.6140)

(a) Gabor + Wavelet + ICA (4 sources)
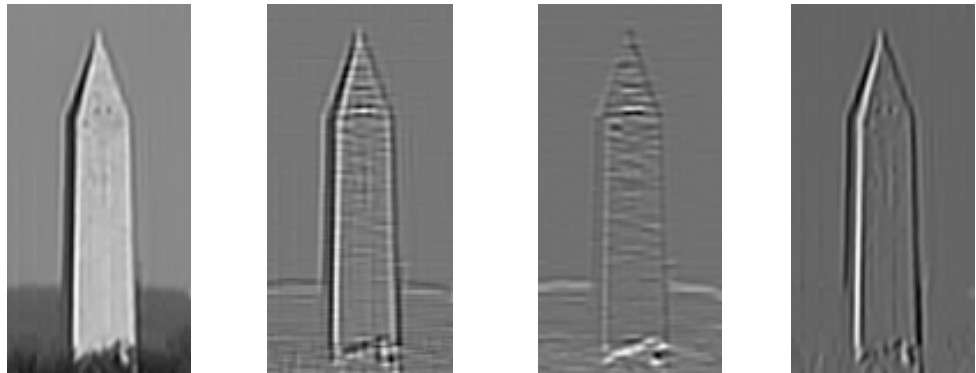
	s_1	s_2	s_3	s_4
Predictability Metric:	(2.0453)	(2.7177)	(2.8131)	(2.1752)

(b) Gabor + Innovation + ICA (4 sources)
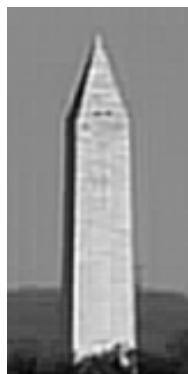
(c) Gabor + Innovation + ICA (1 source)

Fig. 15. Image enhancement for Fig. 13 using single-frame multi-channel filtering.

(a) an original frame

(b) restored image (JADE)

(c) restored image (HP-JADE)

(d) restored image (IN-JADE)

(e) enhanced image for (d)

Fig. 16. Results for real data experiment 2